



# Morphosynthesis of SnO<sub>2</sub> nanocrystal networks as high-capacity anodes for lithium ion batteries

Xiaolei Sun<sup>1,2</sup>

Received: 24 March 2020 / Revised: 29 March 2020 / Accepted: 29 March 2020 / Published online: 13 April 2020  
© Springer-Verlag GmbH Germany, part of Springer Nature 2020

## Abstract

Tin dioxide (SnO<sub>2</sub>) is of interest as an alternative anode material for lithium ion batteries. However, the major concern is the significant volume expansion during lithiation process, resulting in poor capacity retention and rate capability. Here, a facile morphosynthesis route is adapted for the fabrication of hierarchical SnO<sub>2</sub> nanocrystal networks with interwoven fibers, by immersing sacrificial eggshell membrane in a Sn-based sol followed by a calcination process in air. With both structural and compositional advantages, the synthesized SnO<sub>2</sub> networks electrode manifests superior reversible capacities of 938, 802, 736, 636, and 506 mAh g<sup>-1</sup> even at high current densities of 0.2, 0.5, 1, 2, and 5 A g<sup>-1</sup>, respectively. Besides, its initial Coulombic efficiency (72.6%) is also much enhanced compared with that of bare SnO<sub>2</sub> nanoparticles (59.6%) and commercial SnO<sub>2</sub> nanopowders (46.8%). The finding highlights the probable potential application of the SnO<sub>2</sub> networks for next-generation lithium ion batteries.

**Keywords** Tin dioxide · Hierarchical structure · Lithium storage · Electrochemical performance

## Introduction

New functional materials are vital to advances in energy conversion and storage for meeting the challenges of the global energy crisis and related issues [1–6]. So far, significant progress has been done to develop high-performance electrode materials for different types of energy storage devices, such as lead-acid, nickel-cadmium, nickel-metal hydride, and lithium-based batteries [7–11]. Among these, rechargeable lithium ion batteries (LIBs) have boosted the development of portable electronics market and have now been expanded into larger units such as burgeoning plug-in hybrid electric vehicles [12–14]. In terms of Li<sup>+</sup> storage capacity, tin dioxide (SnO<sub>2</sub>) has emerged as an alternative anode for next-

generation LIBs due to its high theoretical capacity (781 mAh g<sup>-1</sup>) and low operation voltage [15–18]. Unfortunately, similar to other high-capacity electrode materials (silicon, germanium), the major concern is the extreme volume change and stress (over 300%), concomitant with Li<sup>+</sup> insertion/extraction, which can induce cracking/pulverization, resulting in electrically disconnected active electrode. Previous studies have identified that bulk and/or micrometer sized SnO<sub>2</sub> particles electrodes only have modest lithium storage capabilities with short battery lifetime, which keeps them from being used in real life LIB applications [19–21].

In the years since the advent of nanotechnology and incorporation of nanostructured materials in a variety of electrochemical devices, many researchers have focused on the morphological and structural modification of materials in order to cope up their electrochemical disadvantages [22–27]. Then various morphologies of SnO<sub>2</sub> structures, including nanoparticles [28], nanowires [29], nanosheets [30], nanotubes [31], and nanospheres [32], have been successfully obtained. Through nanostructuring, the active SnO<sub>2</sub> electrode could minimize the solid-state diffusion lengths for both Li<sup>+</sup> and e<sup>-</sup> because of their confinement effect, improve lithium storage capability, and eventually enhance electrochemical performance [16, 23, 33]. Thus, it is suggested that the structural modification might be an appropriate strategy

✉ Xiaolei Sun  
xiaolei.sun@nankai.edu.cn

<sup>1</sup> Tianjin Key Lab for Rare Earth Materials and Applications, Centre for Rare Earth and Inorganic Functional Materials, School of Materials Science and Engineering & National Institute for Advanced Materials, Nankai University, Tianjin 300350, People's Republic of China

<sup>2</sup> Key Laboratory for Magnetism and Magnetic Materials of the Ministry of Education, Lanzhou University, Lanzhou 730000, People's Republic of China

to minimize the pulverization of SnO<sub>2</sub> electrodes, yielding stable capacity retention [34–36]. Therefore, finding an efficient synthetic method for low-cost and high-performance SnO<sub>2</sub> anode material has always been greatly attractive but very challenging.

Most encouragingly, a few recent reports on morphosynthesis have documented that it could be an effective method to control particle morphology through selecting suitable sacrificial templates [37–39]. Biotemplates such as eggshell membrane (ESM), which has a porous interwoven fibrous structure, are suitable for making nanoscale inorganic metal oxide materials because strong metal-protein binding can be advantageously utilized [40–43]. In this work, hierarchical SnO<sub>2</sub> networks with interwoven fibers comprising tetragonal rutile nanocrystals were successfully synthesized, using a sol-gel method with biological ESM as a template. When used as an anode material for lithium storage, the SnO<sub>2</sub> networks electrode possesses several advantageous features such as high reversible capacity (855 mAh g<sup>-1</sup>), improved cycling stability, and excellent rate capability. Besides, its initial Coulombic efficiency (72.6%) is also much enhanced compared with that of bare SnO<sub>2</sub> nanoparticles (59.6%) and commercial SnO<sub>2</sub> nanopowders (46.8%).

## Experimental section

### Preparation of samples

The SnO<sub>2</sub> nanocrystal networks were fabricated by immersing eggshell membrane (ESM) sacrificial template in a Sn-based sol with subsequent calcination treatment. In a typical experiment, a sol was obtained by dissolving 6 mmol of SnCl<sub>2</sub>·2H<sub>2</sub>O in a solvent mixture composed of 1.88 mL ethanol and 0.12 mL of hydrochloric acid (37%) to yield a 3 M Sn<sup>2+</sup> solution, which was further aged for 24 h. Then deionized (DI) water (0.12 mL) was added and aged for 24 h again to yield a transparent sol. The inner membrane was manually separated from commercial eggshell. The obtained ESM was cleaned with DI water and dried at 40 °C for 6 h. A separate piece of the dried membrane was immersed into the aforementioned sol for 12 h at 30 °C. Subsequently, the saturated membrane was rinsed several times with DI water to remove the residual nanoparticle debris and subsequently dried in vacuum at 40 °C for 6 h. Then, the resulting product was further calcined in a tube furnace at 700 °C in air atmosphere for 2 h with a heating rate of 2 °C min<sup>-1</sup> to obtain the SnO<sub>2</sub> nanocrystal networks. For comparison, the sol-gel prepared SnO<sub>2</sub> nanoparticles were directly obtained under similar experimental conditions without ESM biotemplate, and the commercial SnO<sub>2</sub> nanopowders (50–70 nm, 99.9%) were purchased from Aladdin Reagent Co. Ltd.

### Sample characterizations

The microstructure and chemical composition of the samples were thoroughly characterized by X-ray powder diffractometer (XRD, Rigaku RINT2400 with Cu K $\alpha$  radiation;  $\lambda$  = 1.5418 Å), field-emission scanning electron microscope (FE-SEM, Hitachi, S-4800), and transmission electron microscope (TEM, FEI, Tecnai G<sup>2</sup> F30) equipped with energy dispersive X-ray (EDX) spectroscopy, respectively. UV-Visible absorption spectrum was recorded using a Shimadzu UV-3600 UV-Visible spectrophotometer in the range of 200–900 nm. Photoluminescence (PL) measurement was performed on a Jobin Yvon LabRAM HR800 UV micro-Raman spectrometer with a 325 nm line of 50 mW diode-pumped solid-state laser at room temperature. Thermogravimetric analysis (TGA) was conducted in air at a heating rate of 5 °C min<sup>-1</sup> on a Perkin Elmer Diamond TG/DTA instrument.

### Electrochemical measurements

The electrochemical experiments were performed using Swagelok-type cells, with lithium foil as counter and reference electrode at room temperature. The working electrode was prepared by spreading active material (80 wt%), sodium alginate (10 wt%), and carbon black (10 wt%) onto a copper foil substrate and dried in a vacuum oven at 80 °C for 12 h. The Swagelok-type cells assembled process was completed in an argon atmosphere glove box (H<sub>2</sub>O < 0.1 ppm, O<sub>2</sub> < 0.1 ppm, MBraun, Germany). The used electrolyte solution was made of 1 M LiPF<sub>6</sub> dissolved in a mixture of ethylene carbonate, dimethyl carbonate, and ethyl methyl carbonate (1:1:1 by volume) solvent mixtures. Note the accurate amount of electrolyte added to each Swagelok-type cells was 100  $\mu$ L with a micro-syringe. Celgard 2320 microporous polypropylene film was employed as a separator. After assembly, all cells were rested for 10 h to ensure good soaking of the electrolyte solution. Then the cells were galvanostatically measured in the voltage range of 0.01–3.0 V vs. Li/Li<sup>+</sup> using a NEWARE battery tester. The loading amount of active materials for all electrodes was 1.0  $\pm$  0.1 mg cm<sup>-2</sup>. Cyclic voltammetry (CV) were performed with a scan rate of 0.2 mV s<sup>-1</sup> between 0.01 and 3.0 V. In electrochemical impedance spectroscopy (EIS) measurement, the impedance spectra were recorded at the open circuit potential in a frequency range from 10<sup>5</sup> to 10<sup>-2</sup> Hz with an amplitude of the alternating voltage signal of 5 mV, which was stabilized by 30 min of rest to reach a stable state about 1.9 V. Both the CV and EIS measurements were finished with a CHI 660C electrochemical analyzer at room temperature. The Coulombic efficiency was defined as 100% ( $C^{\text{dealloy}}/C^{\text{alloy}}$ ), where  $C^{\text{alloy}}$  and  $C^{\text{dealloy}}$  were the values of discharge and charge capacities, respectively.

## Results and discussion

It is well-known that natural ESM has abundant amines, amides, and carboxylic surface functional groups [40]. These complexes are able to interact with the transparent Sn sol, thus promoting the homogeneous distribution of the precursor molecules on membrane fiber surface. Thermogravimetric analysis (TGA) curves of the ESM template and the ESM coated with Sn gel (ESM-Sn hybrids) are both displayed in Fig. 1. The weight losses before 100 °C are related to the removal of water weakly adsorbed to the surfaces of the two samples. The blank ESM template starts pyrolyzing at around 225 °C, which corresponds to the charring of the abovementioned organic constituents, and is completely pyrolyzed at 600 °C. However, the ESM-Sn hybrids are thoroughly pyrolyzed at 650 °C, which may be due to the decomposition of inorganic matters at higher temperatures, and remained up to 40.6 wt%.

Figure 2a displays XRD patterns of the bare ESM template, the ESM-Sn hybrids before and after calcination at 700 °C for 2 h in air. The first broad peak around 23° corresponds to the ESM reflection. It can be easily found that without calcination, tin species occurrence in the ESM-Sn hybrids are almost amorphous, which might be derived from the organic matters of the ESM template [43]. In fact, there still exist some diffraction peaks that belong to tin dioxide, suggesting that small crystalline SnO<sub>2</sub> phase could be generated at a room temperature sol-gel process. After calcination in air at 700 °C, the amorphous tin species crystallize into tetragonal rutile like SnO<sub>2</sub> structure with P42/mnm space group (JCPDS card no. 41-1445), accompanying the complete ESM template pyrolysis. No other diffraction peaks could be detected for impurities such as tin or other tin oxides, implying the formation of an oxide phase with a tetragonal rutile structure. The average crystal sizes of the sample are calculated to be about 20 nm,

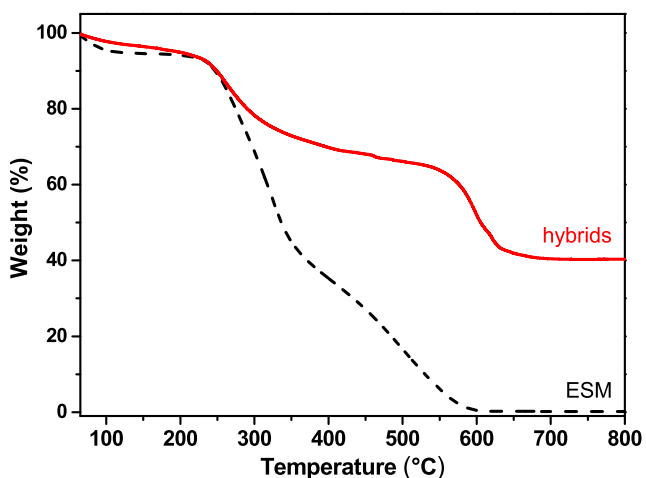


Fig. 1 TGA curves of natural ESM template and saturated ESM-Sn hybrids before calcination

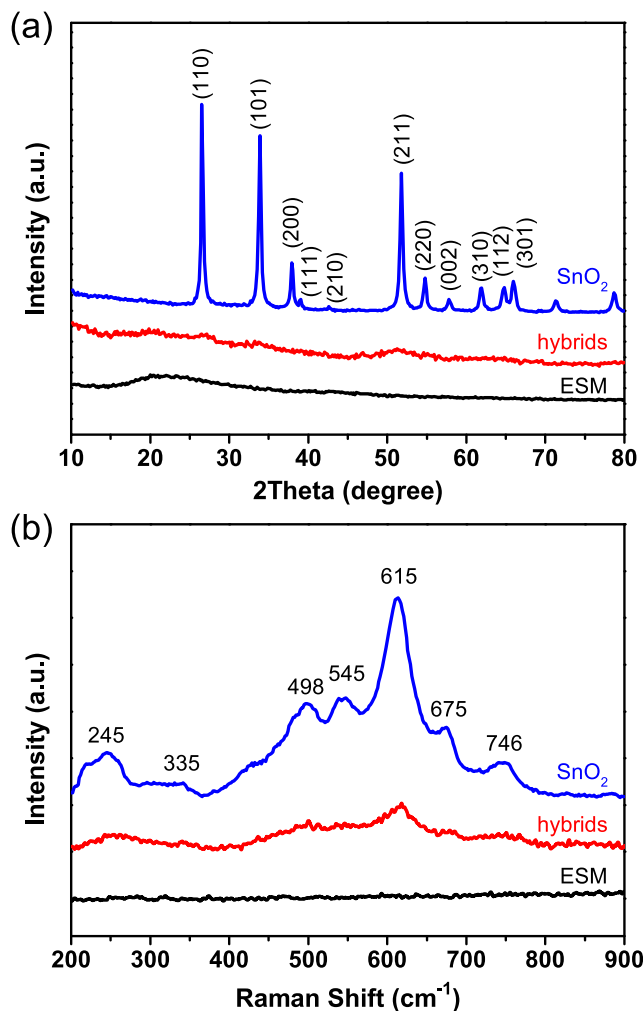


Fig. 2 a XRD patterns and b Raman spectra of ESM template, ESM-Sn hybrids before and after calcination at 700 °C in air

which is based on the line-width analysis of the tetragonal (110) diffraction peak using Scherrer equation.

Typical Raman spectra of the ESM-Sn hybrids with and without calcination treatment, as well as the bare ESM template are presented in Fig. 2b. It can be observed that there are no features in the spectrum of the natural ESM matter, while, for the ESM-Sn hybrids, fairly broad low intensity peaks are exhibited, demonstrating that the unheated samples are mainly amorphous according to the Raman measurements. Expectedly, the intensities of these primary peaks become much stronger and could be defined after being calcined at 700 °C, without shifting position. Note that also the heated samples show stronger peak intensity than those of the ESM-Sn hybrids, which is attributed to better crystallization and larger grain size at high reaction temperature. Classically, rutile SnO<sub>2</sub> has been thought to belong to the space group *D*<sub>4h</sub>. On the basis of group theory, the normal lattice vibration modes at the  $\Gamma$  point of the Brillouin zone could be expressed using the following equation:

$$\Gamma = 1A_{1g} + 1A_{2g} + 1A_{2u} + 1B_{1g} + 1B_{2g} + 2B_{1u} + 1E_g + 3E_u.$$

Among them, Raman active vibrational modes are identified and assigned to  ${}^1A_{1g}$ ,  ${}^1B_{1g}$ ,  ${}^1B_{2g}$ , and  ${}^1E_g$  only [44]. In detail, the three peaks at 498, 615, and 746  $\text{cm}^{-1}$  are attributed to the  $E_g$ ,  $A_{1g}$ , and  $B_{2g}$  vibrational modes of tetragonal  $\text{SnO}_2$ , respectively [45, 46]. The peak observed at 675  $\text{cm}^{-1}$  is due to the characteristic  $A_{2u}$  mode. Another low intensity peak at 545  $\text{cm}^{-1}$  is near the characteristic of amorphous  $\text{SnO}_2$  peak at 566  $\text{cm}^{-1}$  as reported previously [45]. Finally, two peaks are observed at 245 and 335  $\text{cm}^{-1}$ , and could be associated with the IR active  $E_u$  modes [28, 47]. Therefore, all these aforementioned features confirm the tetragonal rutile structure of the resultant  $\text{SnO}_2$  sample.

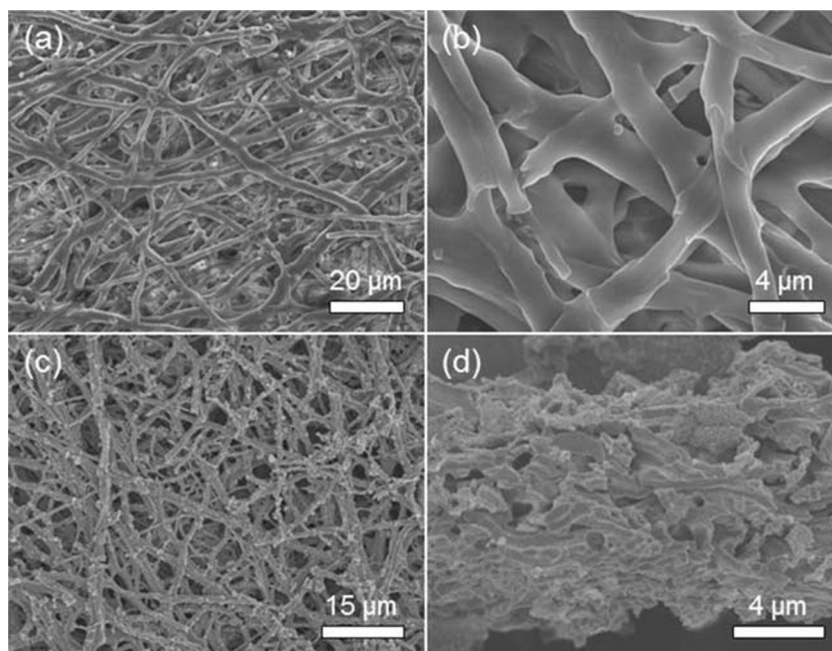
The morphologies of the original ESM template and the synthesized  $\text{SnO}_2$  samples were investigated using field-emission scanning electron microscope (FE-SEM), and the results of the observations are given in Fig. 3. As illustrated in Fig. 3a, b, the initial membrane template has a unique cross-stacked microstructure, which is composed of ESM fibers ranging from 2 to 4  $\mu\text{m}$  in diameter. Furthermore, these fibers have core-shell structures consisting of rich glycoprotein and collagen components [40]. Generally speaking, after the ESM-Sn hybrids were calcined at 700  $^\circ\text{C}$ , the membrane-like structure would shrink and wrinkle to some extent, but the crack-free shape would be well preserved. Typical SEM micrographs of the ESM-morphic  $\text{SnO}_2$  resultants after being held at 700  $^\circ\text{C}$  for 2 h are shown in Fig. 3c, d. Overall, the findings indicate that the continuous network structure of the ESM template is well kept. As seen in Fig. 3c, the as-synthesized  $\text{SnO}_2$  products have interwoven and coalescing fibers with diameter ranging from 1 to 2  $\mu\text{m}$ , which is somewhat smaller than the normal membrane fibers (2–4  $\mu\text{m}$ ). Figure 3d provides more detailed morphological study of the

samples by revealing visual representations based on cross-section analysis. It is apparent that the  $\text{SnO}_2$  networks are consisted of tubes with wall of around 15- $\mu\text{m}$  thickness.

Typical transmission electron microscopy (TEM) analysis of the interconnected  $\text{SnO}_2$  networks is displayed in Fig. 4a, b. Obviously, the tubular wall consists of quasi-continuous nanocrystals (18–23 nm), which is identical with the XRD results. The corresponding ring-like selected area electron diffraction (SAED) pattern derived from the framed area in Fig. 4a indicates that the obtained  $\text{SnO}_2$  fibers comprise nanocrystals. The arranged diffraction rings are accurately assigned to (110), (101), (200), (111), (211), and (112) lattice planes of rutile phase  $\text{SnO}_2$ , respectively. Moreover, high-resolution TEM image (Fig. 4d) and the corresponding fast Fourier-transform (FFT) patterns given in Fig. 4e collected in different zones demonstrate that the  $\text{SnO}_2$  sample is composed of nanoscaled  $\text{SnO}_2$  particles surrounded by amorphous matrices. The lattice fringes marked by arrows have an interplanar spacing of 0.33 nm for tetragonal rutile  $\text{SnO}_2$  (110) lattice. The FFT pattern illustrated in Fig. 4e (left) could be indexed to the diffraction spots of the [001] zone, which is oriented along electron beam direction. Thus, it is evident that the  $\text{SnO}_2$  nanocrystals are exposed with high energy (001) facets, which are beneficial to high lithium storage performance.

As depicted in Fig. 5, chemical composition of the as-synthesized materials was further determined by energy dispersive X-ray (EDX) spectroscopy. The EDX spectrum performed on nanocrystals confirms the simultaneous presence of tin and oxygen (note that the copper peaks come from the copper TEM grid). Note the EDX measurements on different spots of the samples always give the same results, which

**Fig. 3** a, b Typical FE-SEM images of original ESM template. c, d Top and cross-sectional view of as-synthesized  $\text{SnO}_2$  samples



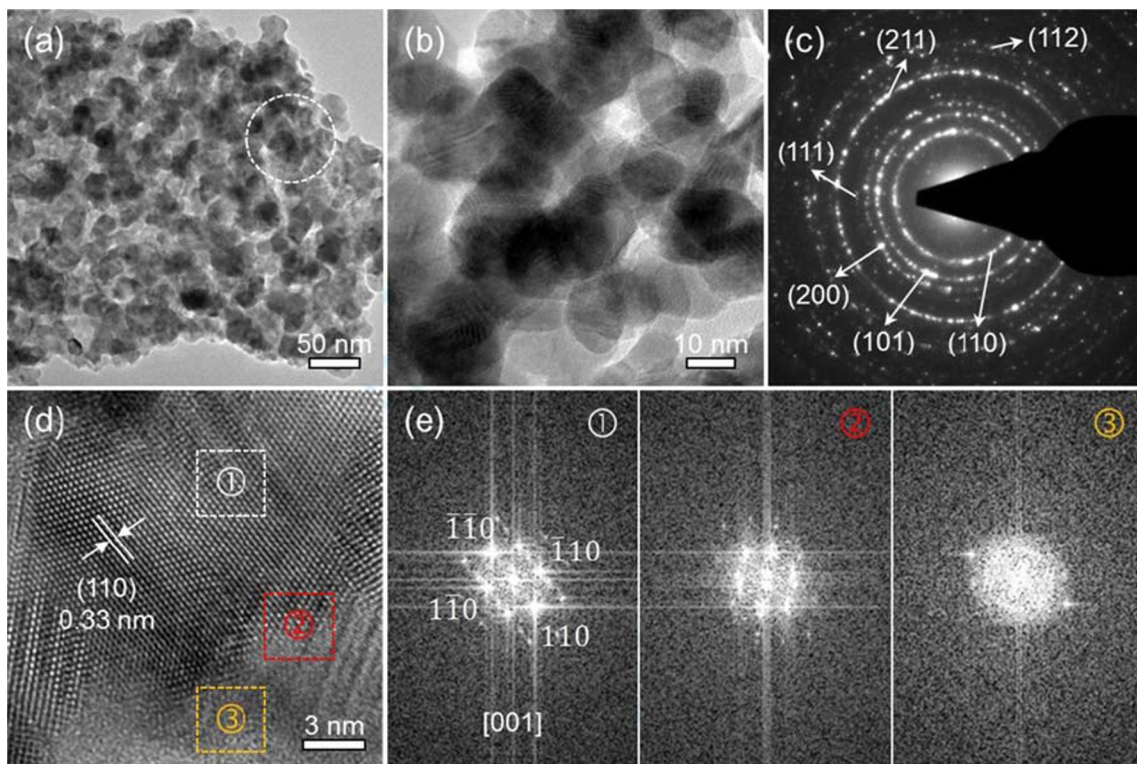


**Fig. 4** **a, b** Representative TEM images, **c** SAED pattern, **d** high-resolution TEM image of SnO<sub>2</sub> networks annealed in air at 700 °C. **e** The corresponding fast Fourier-transform (FFT) patterns of the same regions indicated by the squares

illustrate good homogeneity of the specimens. The semi-quantitative assessment indicates that the as-synthesized ESM-morphic SnO<sub>2</sub> networks contain approximately 61 at% oxygen and 39 at% tin, which indicates a high ratio of oxygen vacancies (V<sub>o</sub><sup>+</sup> or V<sub>o</sub><sup>++</sup>) in the interior and surface of the products caused by heat-treatment. In some respects, these defects are expected to be beneficial for increasing electrochemical performance of battery materials [48–51].

Optical properties of the as-prepared SnO<sub>2</sub> networks were further characterized by UV-Vis absorption spectrum and the

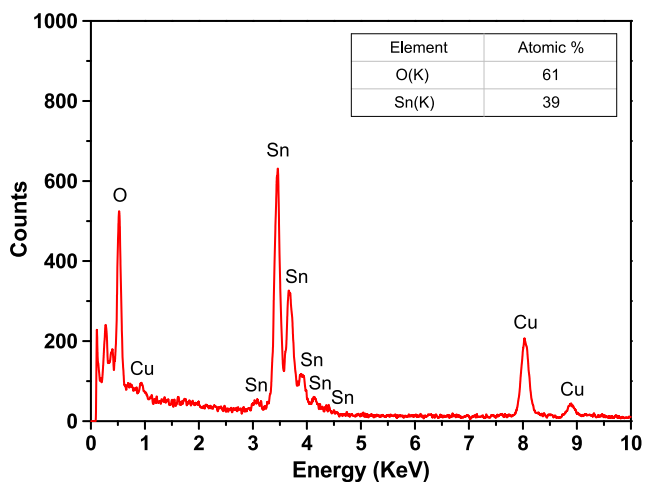


**Fig. 5** EDX spectrum of SnO<sub>2</sub> networks annealed in air at 700 °C. Copper signals are attributed to the supporting TEM copper grid

results are displayed in Fig. 6a. It is found that the SnO<sub>2</sub> networks have high absorption ability particularly at wavelengths shorter than 400 nm, which could be attributed to the intrinsic band gap absorption. The steep band edge demonstrates that the light absorption is related to the band gap transition rather than the transition from impurity level [52]. The optical band gap ( $E_g$ ) can be easily deduced from the equation of  $(\alpha h\nu)^2 = A(h\nu - E_g)$ , where  $h\nu$  is photo energy,  $\alpha$  is absorption coefficient, and  $A$  is a constant for semiconductor material [53]. As plotted in the inset of Fig. 6a, the  $E_g$  value can be estimated to be about 3.62 eV. Compared with bulk SnO<sub>2</sub> ( $E_g = 3.6$  eV), the band gap for the SnO<sub>2</sub> networks manifests a blue shift, which might be related to the size effect of crystals and the presence of oxygen vacancies.

Figure 6b exhibits photoluminescence (PL) spectrum of the SnO<sub>2</sub> networks at room temperature, where the excitation wavelength is 325 nm. Through multi-peak Gaussian fitting, it is clear that the broad band is composed of three peaks, which are centered at about 421, 544, and 628 nm, respectively. The strong green emission peak at ~544 nm is assigned to metastable energy levels associated with oxygen vacancies [54]. The broad red emission peak at ~628 nm might be raised from a transition of the oxygen vacancy defect states located at the band gap [55]. In addition, it is noticed that there is a small emission peak at ~421 nm, indicating the existence of oxygen-related defects [56]. To sum up the above results, the bulk oxygen species formed at the surface and in the

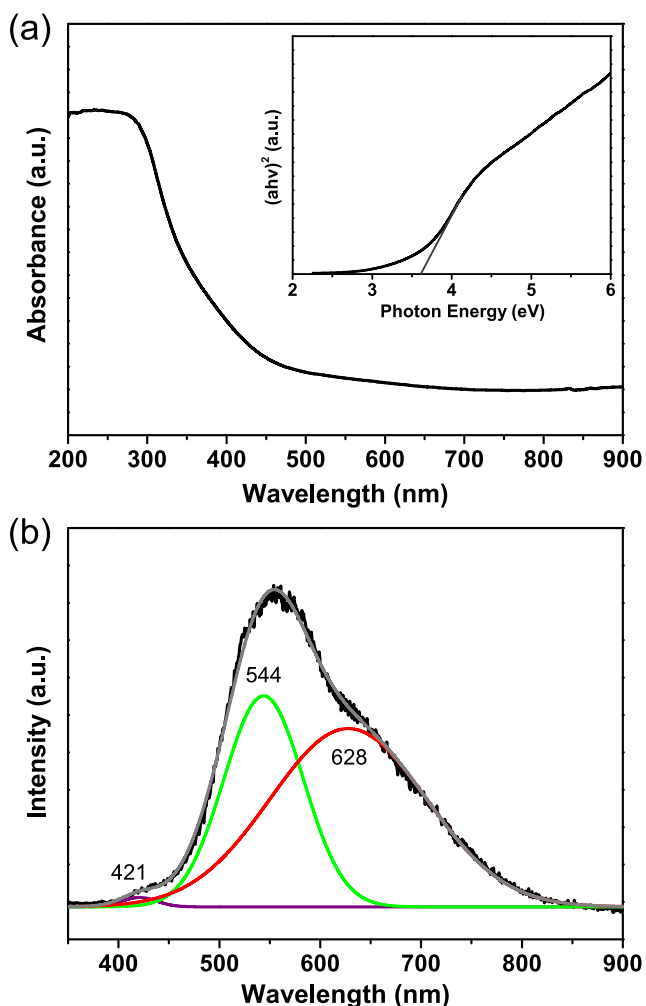


**Fig. 6** **a** UV-Vis absorption spectrum and a plot of  $(\alpha h\nu)^2$  vs. photon energy ( $h\nu$ ) (inset), and **b** PL spectrum of  $\text{SnO}_2$  networks

interior of the sample may have relatively high mobility, which can facilitate  $\text{Li}^+$  insertion/extraction and further lead to an improved electrochemical performance.

Furthermore, to investigate the lithium storage properties of the obtained  $\text{SnO}_2$  networks, Swagelok-type cells were assembled with lithium foil serves as counter and reference electrode. Figure 7a represents the initial five consecutive cyclic voltammetry (CV) profiles of the  $\text{SnO}_2$  networks electrode at a scan rate of  $0.2 \text{ mV s}^{-1}$  within a voltage window of 0.01–3.0 V, which are generally consistent with previous observations [23, 57], indicating a similar electrochemical pathway. In the first cathodic process, two main reduction peaks are observed, which are located at 0.75 and 0.16 V. The former peak at 0.75 V corresponds to the initial reduction of  $\text{SnO}_2$  to Sn according to  $\text{SnO}_2 + 4\text{Li}^+ + 4\text{e}^- \rightarrow \text{Sn} + 2\text{Li}_2\text{O}$ , the decomposition of electrolyte, and the formation of solid electrolyte interphase (SEI) layer. The latter peak at 0.16 V is assigned to the well-known multi-step formation of different Li-Sn alloys ( $\text{Li}_2\text{Sn}_5$ , Li-Sn,  $\text{Li}_7\text{Sn}_3$ ,  $\text{Li}_5\text{Sn}_2$ ,  $\text{Li}_{22}\text{Sn}_5$ ) according to  $\text{Sn} + x\text{Li} + x\text{e}^- \rightarrow \text{Li}_x\text{Sn}$ . The oxidation peaks from 0.28

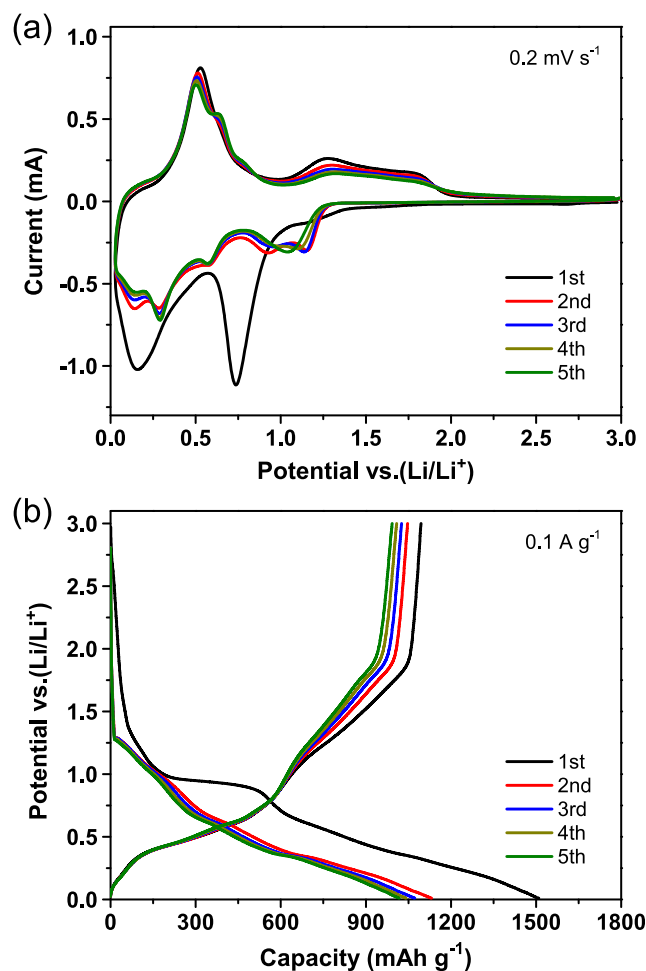


**Fig. 7** Electrochemical behaviors of  $\text{SnO}_2$  networks electrodes. **a** CV profiles of the initial five cycles at a scan rate of  $0.2 \text{ mV s}^{-1}$  between 0.01 and 3.0 V. **b** Discharge/charge voltage profiles at a current density of  $0.1 \text{ A g}^{-1}$  within a voltage window of 0.01–3.0 V for the first five cycles

to 0.85 V in the subsequent anodic process can be related to the de-alloying of  $\text{Li}_x\text{Sn}$ . However, an interesting phenomenon found here is that the CV curves in the following cycles remain similar without obvious changes, indicating that the  $\text{SnO}_2$  networks electrode has good lithium storage reversibility.

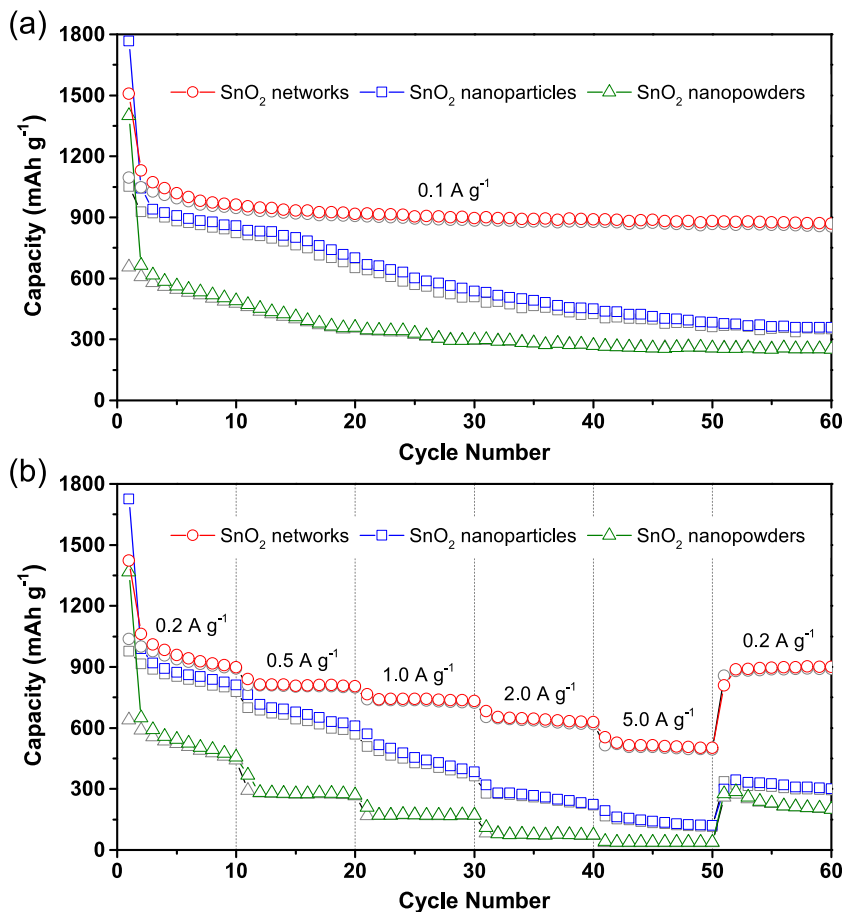
Figure 7b displays representative galvanostatic discharge/charge curves under a constant current density of  $0.1 \text{ A g}^{-1}$  in the same potential window of 0.01–3.0 V for the initial five cycles. As a result, a discharge plateau between 1.0 and 0.8 V only presents in the first cycle and then disappears in the subsequent cycles, which can be related to the decomposition of  $\text{SnO}_2$  to Sn, and the formation of the SEI layer. Furthermore, the voltage region below 0.8 V is attributed to the continuous multi-step reactions of Li-Sn alloys. The corresponding regions of the charge curves along with delithiation reactions can also be found. These similar features are also in accordance with the CV results. Meanwhile, the initial discharge capacity and charge capacity are calculated to

be 1507 and 1094 mAh g<sup>-1</sup>, respectively, which corresponds to an initial Coulombic efficiency of 72.6%. This observed irreversible capacity loss is possible as the result of the large number of Li<sup>+</sup> consumed to form Sn, Li<sub>2</sub>O, and Li-Sn alloys. It is suggested that the partial decomposition of Li<sub>2</sub>O, interfacial charge storage, and reversible side reactions could contribute to the total lithium storage properties in terms of superior capacity and initial Coulombic efficiency, which has also been found in other materials [32, 58–61].

The galvanostatic method was used to further investigate the long-term cycling behavior of the SnO<sub>2</sub> networks electrode at a current density of 0.1 A g<sup>-1</sup> with a fixed voltage window between 0.01 and 3.0 V. As shown in Fig. 8a, the obtained SnO<sub>2</sub> networks exhibit larger capacity and better capacity retention than that of the SnO<sub>2</sub> nanoparticles and the SnO<sub>2</sub> nanopowders. Obviously, the reversible capacity of the SnO<sub>2</sub> networks electrode just slightly decreases in the first few cycles and then remains constant, maintaining a high-level of charge capacity. After 60 discharge/charge cycles, a high reversible capacity of 855 mAh g<sup>-1</sup> for the SnO<sub>2</sub> networks electrode, while the corresponding values of the SnO<sub>2</sub> nanoparticles and SnO<sub>2</sub> nanopowders are only 350 and 251 mAh g<sup>-1</sup>, respectively, because of their much faster capacity fading.

To further evaluate the rate capabilities, the three samples were cycled at various discharge/charge current densities ranging from 0.2 to 5 A g<sup>-1</sup>, as given in Fig. 8b. Although the capacities decrease with increasing current densities, the SnO<sub>2</sub> networks still exhibit high reversible capacities of 938, 802, 736, 636, and 506 mAh g<sup>-1</sup> at the current densities of 0.2, 0.5, 1, 2, and 5 A g<sup>-1</sup>, respectively. However, the SnO<sub>2</sub> nanoparticles exhibit moderate reversible capacities of 851, 642, 427, 258, and 134 mAh g<sup>-1</sup> at the current densities of 0.2, 0.5, 1, 2, and 5 A g<sup>-1</sup>, respectively. The SnO<sub>2</sub> nanopowders exhibit low reversible capacities of 523, 273, 173, 74, and 36 mAh g<sup>-1</sup> at the current densities of 0.2, 0.5, 1, 2, and 5 A g<sup>-1</sup>, respectively. The rate capacity retentions of the SnO<sub>2</sub> networks, the SnO<sub>2</sub> nanoparticles, and the SnO<sub>2</sub> nanopowders are 54%, 16%, and 7%, respectively, when the current density rises from 0.2 to 5 A g<sup>-1</sup>. More importantly, when the current density is set to the initial value of 0.2 A g<sup>-1</sup>, the SnO<sub>2</sub> networks electrode could resume its original charge capacity of about 887 mAh g<sup>-1</sup>, that is, a value almost 2.5 times larger than that of the theoretical maximum capacity for graphite (372 mAh g<sup>-1</sup>). The results suggest that the SnO<sub>2</sub> networks remain exceedingly stable even under high rate discharge/charge cycling conditions. In contrary, both the SnO<sub>2</sub> nanoparticles and the SnO<sub>2</sub> nanopowders display

**Fig. 8** a Cycle performance and b rate capability of SnO<sub>2</sub> networks, SnO<sub>2</sub> nanoparticles, and SnO<sub>2</sub> nanopowders at various current densities with a cutoff voltage window of 0.01 to 3.0 V



inferior rate capabilities and lower reversible capacities when the current density is again reduced back to  $0.2 \text{ A g}^{-1}$ .

Electrochemical impedance spectra (EIS) of the  $\text{SnO}_2$  networks electrode were measured to further elucidate the intrinsic electrochemical and kinetic mechanisms. Figure 9a presents Nyquist impedance plots of the  $\text{SnO}_2$  networks electrode, which were discharged/charged at a constant current density of  $0.1 \text{ A g}^{-1}$  after different cycles. As can be viewed, all impedance spectra show similar features, consisting of a depressed semicircle in high-to-medium frequencies, and an inclined line in low frequency, which is in consistent with previous investigations [62]. The depressed semicircle reflects the resistance from the processes of  $\text{Li}^+$  diffusion in the surface film and the charge transfer across the electrode interface, whereas the inclined line represents  $\text{Li}^+$  diffusion resistance in the electrode. The observed trends suggest that the cell impedance undergoes an increment of cycle processes, which has been observed in other materials [63]. In some previous studies, the cell impedance might decrease after many cycles,

which could be assigned to the formed small particles during the pulverization process. Because of the large surface energy, these small particles would be induced to agglomerate into large clusters, leading to rapid capacity decay and reduced lifetime. In the present work, the hierarchical nanocrystal networks structure is more stable than nanoparticles and nanopowders. This spatial confinement effect should be beneficial for reducing the milling effect on the elongation of lithium storage time, and then ensuring long battery lifetime. Figure 9b further depicts the corresponding Bode plots of the  $\text{SnO}_2$  networks electrode. This analysis reveals that the high frequency impedances (above  $10^2 \text{ Hz}$ ) remain constant with cycles, while those low frequencies impedances (below  $10^2 \text{ Hz}$ ) are slowly increased with cycles.

The exceptional electrochemical performance of the  $\text{SnO}_2$  networks is due to several factors. First, the unique interwoven structure could limit the mobility of active particles during repeated cycling, and therefore, the agglomeration effect will be minimized. Second, the interconnected framework structure can provide a sufficient space to accommodate the volume change during lithiation/delithiation process. Third, the nanoscale dimension of interconnected  $\text{SnO}_2$  nanocrystals could provide short solid-state diffusion length for  $\text{Li}^+$  insertion, which is beneficial for retaining good structural stability and excellent rate capability. Fourth, the hierarchical networks could promote liquid electrolyte diffusion into the bulk of the electrode, resulting in improved  $\text{Li}^+$  diffusion kinetics. Last but not least, the subsistent oxygen vacancies ( $\text{V}_\text{o}^+$  or  $\text{V}_\text{o}^{++}$ ) in the interior and surface of the  $\text{SnO}_2$  networks may play an active role in interfacial charge storage and reversible side reactions, which has been also demonstrated in many other oxide electrodes [64–66].

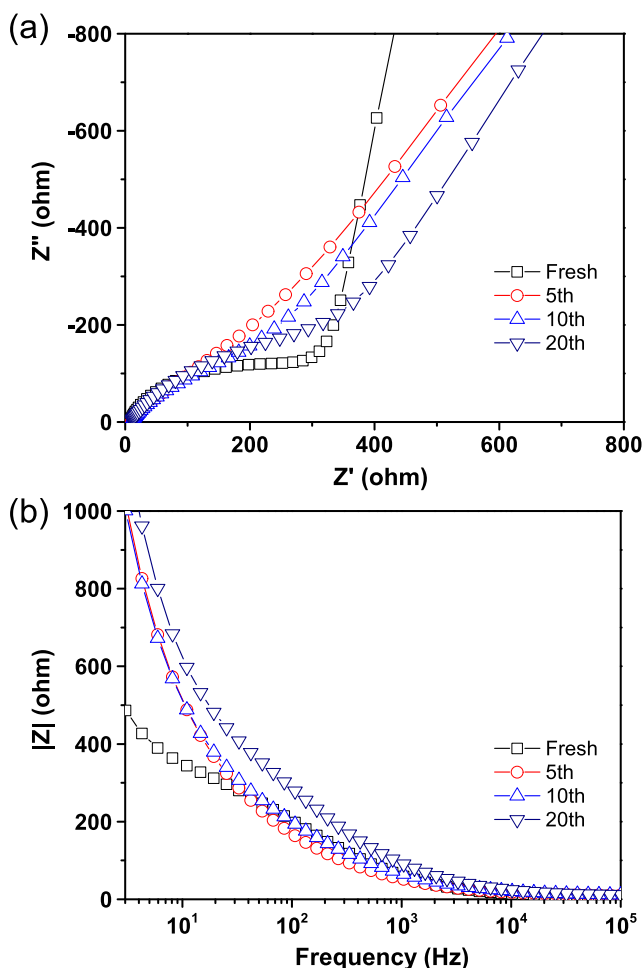


**Fig. 9** Electrochemical impedance spectra of  $\text{SnO}_2$  networks electrode. **a** Nyquist impedance spectra and **b** the corresponding Bode plots of  $\text{SnO}_2$  networks electrode after different cycles of discharge/charge at a current density of  $0.1 \text{ A g}^{-1}$

## Conclusions

In summary, the present work provides a feasible strategy to fabricate hierarchical  $\text{SnO}_2$  nanocrystal networks by immersing sacrificial eggshell membrane in a Sn-based sol with subsequent calcination treatment. When employed as anode materials, the synthesized  $\text{SnO}_2$  networks electrode exhibits high-capacity retention, improved cycling stability, and excellent rate capability than the  $\text{SnO}_2$  nanoparticles and the commercial  $\text{SnO}_2$  nanopowders. The enhanced lithium storage properties could be attributed to the synergistic coupling effect of the distinctive structural features and nanocrystals with oxygen vacancies, the reduction of  $\text{Li}^+$  diffusion pathways, and the additional interfacial charge storage. The finding highlights the probable potential application of the  $\text{SnO}_2$  networks in LIB anodes. In addition, the inherent characteristics of the hierarchical structure can be easily extended for other oxide micro/nanomaterials, paving the way for energy storage and other applications.



**Authors' contributions** X. Sun designed and carried out all of the experiments, interpreted the results, and wrote the whole manuscript.

**Funding information** This work was supported by grants from the National Natural Science Foundation of China (Grant No. 11904179), the Fundamental Research Funds for the Central Universities, Nankai University, the Basic Scientific Research Business Expenses of the Central University and Open Project of Key Laboratory for Magnetism and Magnetic Materials of the Ministry of Education, Lanzhou University (Grant No. LZUMMM2020006).

**Availability of data and material** All data are fully available without restriction.

## Compliance with ethical standards

**Conflict of interest** The author declares that there is no conflict of interest.

**Code availability** Not applicable.

## References

- Aricò AS, Bruce P, Scrosati B, Tarascon J-M, Van Schalkwijk W (2005) Nanostructured materials for advanced energy conversion and storage devices. *Nat Mater* 4:366–377. <https://doi.org/10.1038/nmat1368>
- Liu B, Yan C, Si W, Sun X, Lu X, Ansorge-Schumacher M, Schmidt OG (2018) Ultralong-discharge-time biobattery based on immobilized enzymes in bilayer rolled-up enzymatic nanomembranes. *Small* 14:1704221. <https://doi.org/10.1002/sml.201704221>
- Zhai X, Zhang P, Liu C, Bai T, Li W, Dai L, Liu W (2012) Highly luminescent carbon nanodots by microwave-assisted pyrolysis. *Chem Commun* 48:7955–7957. <https://doi.org/10.1039/c2cc33869f>
- Wang X, Li X, Sun X, Li F, Liu Q, Wang Q, He D (2011) Nanostructured NiO electrode for high rate Li-ion batteries. *J Mater Chem* 21:3571–3573. <https://doi.org/10.1039/c0jm04356g>
- Zhao Y, Li X, Yan B, Xiong D, Li D, Lawes S, Sun X (2016) Recent developments and understanding of novel mixed transition-metal oxides as anodes in lithium ion batteries. *Adv Energy Mater* 6:1502175. <https://doi.org/10.1002/aenm.201502175>
- Zhou Q, Pu J, Sun X, Zhu C, Li J, Wang J, Chang S, Zhang H (2017) In situ surface engineering of nickel inverse opal for enhanced overall electrocatalytic water splitting. *J Mater Chem A* 5:14873–14880. <https://doi.org/10.1039/c7ta03044d>
- Ren Z, Yu J, Li Y, Zhi C (2018) Tunable free-standing ultrathin porous nickel film for high performance flexible nickel-metal hydride batteries. *Adv Energy Mater* 8:1702467. <https://doi.org/10.1002/aenm.201702467>
- Zhang Y, Tao L, Xie C, Wang D, Zou Y, Chen R, Wang Y, Jia C, Wang S (2020) Defect engineering on electrode materials for rechargeable batteries. *Adv Mater* 1905923. <https://doi.org/10.1002/adma.201905923>
- Sun X, Wang X, Feng N, Qiao L, Li X, He D (2012) A new carbonaceous material derived from biomass source peels as an improved anode for lithium ion batteries. *J Anal Appl Pyrolysis* 100:181–185. <https://doi.org/10.1016/j.jaap.2012.12.016>
- Tang B, Shan L, Liang S, Zhou J (2019) Issues and opportunities facing aqueous zinc-ion batteries. *Energy Environ Sci* 12:3288–3304. <https://doi.org/10.1039/c9ee02526j>
- Zhao Y, Sun X (2018) Molecular layer deposition for energy conversion and storage. *ACS Energy Lett* 3:899–914. <https://doi.org/10.1021/acsenenergylett.8b00145>
- Sun X, Yan C, Chen Y, Si W, Deng J, Oswald S, Liu L, Schmidt OG (2014) Three-dimensionally “curved” NiO nanomembranes as ultrahigh rate capability anodes for Li-ion batteries with long cycle lifetimes. *Adv Energy Mater* 4:1300912. <https://doi.org/10.1002/aenm.201300912>
- Hayner CM, Zhao X, Kung HH (2012) Materials for rechargeable lithium-ion batteries. *Annu Rev Chem Biomol Eng* 3:445–471. <https://doi.org/10.1146/annurev-chembioeng-062011-081024>
- Sun X, Si W, Xi L, Liu B, Liu X, Yan C, Schmidt OG (2015) In situ formed, amorphous, oxygen-enabled germanium anode with robust cycle life for reversible lithium storage. *ChemElectroChem* 2:737–742. <https://doi.org/10.1002/celec.201402404>
- Li NC, Martin CR (2001) A high-rate, high-capacity, nanostructured Sn-based anode prepared using sol-gel template synthesis. *J Electrochem Soc* 148:A164–A170. <https://doi.org/10.1149/1.1342167>
- Tian H, Xin F, Wang X, He W, Han W (2015) High capacity group-IV elements (Si, Ge, Sn) based anodes for lithium-ion batteries. *J Mater* 1:153–169. <https://doi.org/10.1016/j.jmat.2015.06.002>
- Zheng S, Su L, Zheng L, Wu H, Wang L, Zhong H, Ren M, Li M (2020) Sub-10 nm SnO<sub>2</sub>/Fe<sub>3</sub>O<sub>4</sub>/graphene nanosheets: nanocatalysis to improve initial coulombic efficiency for lithium storage. *J Alloys Compd* 816:152624. <https://doi.org/10.1016/j.jallcom.2019.152624>
- Hua X, Shen Y, Shi S (2019) SnO<sub>2</sub> nano-particles imbedded in graphene bulk as anode material for lithium-ion batteries. *Ionics* 25:5769–5778. <https://doi.org/10.1007/s11581-019-03131-0>
- Song H, Li X, Cui Y, Xiong D, Wang Y, Zeng J, Dong L, Li D, Sun X (2015) Controllable lithium storage performance of tin oxide anodes with various particle sizes. *Int J Hydrog Energy* 40:14314–14321. <https://doi.org/10.1016/j.ijhydene.2015.03.168>
- Yu X, Yang S, Zhang B, Shao D, Dong X, Fang Y, Li Z, Wang H (2011) Controlled synthesis of SnO<sub>2</sub>@carbon core-shell nanochains as high-performance anodes for lithium-ion batteries. *J Mater Chem* 21:12295–12302. <https://doi.org/10.1039/c1jm11364j>
- Zhao Y, Li X, Yan B, Li D, Lawes S, Sun X (2015) Significant impact of 2D graphene nanosheets on large volume change tin-based anodes in lithium-ion batteries: a review. *J Power Sources* 274:869–884. <https://doi.org/10.1016/j.jpowsour.2014.10.008>
- Zhang P, Wu X, Zhao Y, Wang L, Su L, Wang Y, Ren M (2017) Ultrahigh reversibility of SnO<sub>2</sub> in SnO<sub>2</sub>@C quantum dots/graphene oxide nanosheets for lithium storage. *Chemistryselect* 2:11853–11859. <https://doi.org/10.1002/slct.201702734>
- Chen JS, Lou XW (2013) SnO<sub>2</sub>-based nanomaterials: synthesis and application in lithium-ion batteries. *Small* 9:1877–1893. <https://doi.org/10.1002/sml.201202601>
- Sun X, Lu X, Huang S, Xi L, Liu L, Liu B, Weng Q, Zhang L, Schmidt OG (2017) Reinforcing germanium electrode with polymer matrix decoration for long cycle life rechargeable lithium ion batteries. *ACS Appl Mater Interfaces* 9:38556–38566. <https://doi.org/10.1021/acsnano.9b07042>
- Guo S, Liang S, Zhang B, Fang G, Ma D, Zhou J (2019) Cathode interfacial layer formation via in situ electrochemically charging in aqueous zinc-ion battery. *ACS Nano* 13:13456–13464. <https://doi.org/10.1021/acsnano.9b07042>
- Zhao Y, Song Z, Li X, Sun Q, Cheng N, Lawes S, Sun X (2016) Metal organic frameworks for energy storage and conversion. *Energy Storage Mater* 2:35–62. <https://doi.org/10.1016/j.ensm.2015.11.005>

27. Liu L, Weng Q, Lu X, Sun X, Zhang L, Schmidt OG (2017) Advances on micro-sized on-chip lithium-ion batteries. *Small* 13: 1701847. <https://doi.org/10.1002/sml.201701847>
28. Etacheri V, Seisenbaeva GA, Caruthers J, Daniel G, Nedelec JM, Kessler VG, Pol VG (2015) Ordered network of interconnected SnO<sub>2</sub> nanoparticles for excellent lithium-ion storage. *Adv Energy Mater* 5:1401289. <https://doi.org/10.1002/aenm.201401289>
29. Lei Y, Du N, Liu W, Wu H, Yang D (2019) Synthesis of Co/SnO<sub>2</sub> core-shell nanowire arrays and their electrochemical performance as anodes of lithium-ion batteries. *Ionics* 25:4651–4658. <https://doi.org/10.1007/s11581-019-03029-x>
30. Zhu Y, Guo H, Zhai H, Cao C (2015) Microwave-assisted and gram-scale synthesis of ultrathin SnO<sub>2</sub> nanosheets with enhanced lithium storage properties. *ACS Appl Mater Interfaces* 7:2745–2753. <https://doi.org/10.1021/am507826d>
31. Li L, Yin X, Liu S, Wang Y, Chen L, Wang T (2010) Electrospun porous SnO<sub>2</sub> nanotubes as high capacity anode materials for lithium ion batteries. *Electrochem Commun* 12:1383–1386. <https://doi.org/10.1016/j.elecom.2010.07.026>
32. Wu N, Du W, Gao X, Zhao L, Liu G, Liu X, Wu H, He Y-B (2018) Hollow SnO<sub>2</sub> nanospheres with oxygen vacancies entrapped by a N-doped graphene network as robust anode materials for lithium-ion batteries. *Nanoscale* 10:11460–11466. <https://doi.org/10.1039/C8NR02290A>
33. Huang M, Sun Y, Guan D, Nan J, Cai Y (2019) Hydrothermal synthesis of mesoporous SnO<sub>2</sub> as a stabilized anode material of lithium-ion batteries. *Ionics* 25:5745–5757. <https://doi.org/10.1007/s11581-019-03127-w>
34. Yang R, Gu Y, Li Y, Zheng J, Li X (2010) Self-assembled 3-D flower-shaped SnO<sub>2</sub> nanostructures with improved electrochemical performance for lithium storage. *Acta Mater* 58:866–874. <https://doi.org/10.1016/j.actamat.2009.10.001>
35. Sun X, Wang X, Qiao L, Hu D, Feng N, Li X, Liu Y, He D (2012) Electrochemical behaviors of porous SnO<sub>2</sub>-Sn/C composites derived from pyrolysis of SnO<sub>2</sub>/poly(vinylidene fluoride). *Electrochim Acta* 66:204–209. <https://doi.org/10.1016/j.electacta.2012.01.083>
36. Wang Q, Xu J, Shen G, Guo Y, Zhao X, Xia Y, Sun H, Hou P, Xie W, Xu X (2019) Large-scale carbon framework microbelts anchoring ultrafine SnO<sub>2</sub> nanoparticles with enhanced lithium storage properties. *Electrochim Acta* 297:879–887. <https://doi.org/10.1016/j.electacta.2018.11.175>
37. Sun Y, Hu X, Yu JC, Li Q, Luo W, Yuan L, Zhang W, Huang Y (2011) Morphosynthesis of a hierarchical MoO<sub>2</sub> nanoarchitecture as a binder-free anode for lithium-ion batteries. *Energy Environ Sci* 4:2870–2877. <https://doi.org/10.1039/c1ee01189h>
38. Zhai X, Ruan C, Ma Y, Cheng D, Wu M, Liu W, Zhao X, Pan H, Lu WW (2018) 3D-bioprinted osteoblast-laden nanocomposite hydrogel constructs with induced microenvironments promote cell viability, differentiation, and osteogenesis both in vitro and in vivo. *Adv Sci* 5:1700550. <https://doi.org/10.1002/advs.201700550>
39. Zan G, Wu Q (2016) Biomimetic and bioinspired synthesis of nanomaterials/nanostructures. *Adv Mater* 28:2099–2147. <https://doi.org/10.1002/adma.201503215>
40. Baláz M (2014) Eggshell membrane biomaterial as a platform for applications in materials science. *Acta Biomater* 10:3827–3843. <https://doi.org/10.1016/j.actbio.2014.03.020>
41. Dong D, Wu Y, Zhang X, Yao J, Huang Y, Li D, Li C-Z, Wang H (2011) Eggshell membrane-templated synthesis of highly crystalline perovskite ceramics for solid oxide fuel cells. *J Mater Chem* 21: 1028–1032. <https://doi.org/10.1039/C0JM03061A>
42. Zhai X, Ma Y, Hou C, Gao F, Zhang Y, Ruan C, Pan H, Lu WW, Liu W (2017) 3D-printed high strength bioactive supramolecular polymer/clay nanocomposite hydrogel scaffold for bone regeneration. *ACS Biomater Sci Eng* 3:1109–1118. <https://doi.org/10.1021/acsbomaterials.7b00224>
43. Dong Q, Su H, Zhang D, Zhu N, Guo X (2006) Biotemplate-directed assembly of porous SnO<sub>2</sub> nanoparticles into tubular hierarchical structures. *Scr Mater* 55:799–802. <https://doi.org/10.1016/j.scriptamat.2006.07.012>
44. Porto SPS, Fleury P, Damen T (1967) Raman spectra of TiO<sub>2</sub>, MgF<sub>2</sub>, ZnF<sub>2</sub>, FeF<sub>2</sub>, and MnF<sub>2</sub>. *Phys Rev* 154:522. <https://doi.org/10.1103/PhysRev.154.522>
45. Kelp G, Tätte T, Pikker S, Mändar H, Rozhin AG, Rauwel P, Vanetsev AS, Gerst A, Merisalu M, Mäeorg U (2016) Self-assembled SnO<sub>2</sub> micro- and nanosphere-based gas sensor thick films from an alkoxide-derived high purity aqueous colloid precursor. *Nanoscale* 8:7056–7067. <https://doi.org/10.1039/c5nr07942j>
46. Sun X, Wang X, Qin Y, Li X, Qiao L, Feng N, Hu D, He D (2012) Synthesis of novel pompon-like porous SnO<sub>2</sub> and its application in lithium-ion battery. *Mater Lett* 66:193–195. <https://doi.org/10.1016/j.matlet.2011.08.084>
47. Dharmaraj N, Kim C, Kim K, Kim H, Suh EK (2006) Spectral studies of SnO<sub>2</sub> nanofibres prepared by electrospinning method. *Spectrochim Acta A* 64:136–140. <https://doi.org/10.1016/j.saa.2005.07.007>
48. Xie W, Wang Q, Wang W, Xu Z, Li N, Li M, Jia L, Zhu W, Cao Z, Xu J (2019) Carbon framework microbelt supporting SnO<sub>x</sub> as a high performance electrode for lithium ion batteries. *Nanotechnology* 30:325405. <https://doi.org/10.1088/1361-6528/ab17f4>
49. Wu Y, Jiang Y, Shi J, Gu L, Yu Y (2017) Multichannel porous TiO<sub>2</sub> hollow nanofibers with rich oxygen vacancies and high grain boundary density enabling superior sodium storage performance. *Small* 13:1700129. <https://doi.org/10.1002/sml.201700129>
50. Han M, Huang J, Liang S, Shan L, Xie X, Yi Z, Wang Y, Guo S, Zhou J (2020) Oxygen defects in β-MnO<sub>2</sub> enabling high-performance rechargeable aqueous zinc/manganese dioxide battery. *iScience* 23:100797. <https://doi.org/10.1016/j.isci.2019.100797>
51. Xie W, Gu L, Xia F, Liu B, Hou X, Wang Q, Liu D, He D (2016) Fabrication of voids-involved SnO<sub>2</sub>@C nanofibers electrodes with highly reversible Sn/SnO<sub>2</sub> conversion and much enhanced coulombic efficiency for lithium-ion batteries. *J Power Sources* 327:21–28. <https://doi.org/10.1016/j.jpowsour.2016.07.030>
52. Sun P, You L, Sun Y, Chen N, Li X, Sun H, Ma J, Lu G (2012) Novel Zn-doped SnO<sub>2</sub> hierarchical architectures: synthesis, characterization, and gas sensing properties. *CrystEngComm* 14:1701–1708. <https://doi.org/10.1039/c1ce06197f>
53. Tauc J, Menth A (1972) States in the gap. *J Non-Cryst Solids* 8-10: 569–585. [https://doi.org/10.1016/0022-3093\(72\)90194-9](https://doi.org/10.1016/0022-3093(72)90194-9)
54. Rani S, Roy SC, Karar N, Bhatnagar MC (2007) Structure, microstructure and photoluminescence properties of Fe doped SnO<sub>2</sub> thin films. *Solid State Commun* 141:214–218. <https://doi.org/10.1016/j.ssc.2006.10.036>
55. Chen H, Wu X, Xiong S, Zhang W, Zhu J (2009) Red photoluminescence mechanism in SnO<sub>2</sub> nanostructures. *Appl Phys A Mater Sci Process* 97:365–368. <https://doi.org/10.1007/s00339-009-5217-z>
56. Her Y-C, Wu J-Y, Lin Y-R, Tsai S-Y (2006) Low-temperature growth and blue luminescence of SnO<sub>2</sub> nanoblades. *Appl Phys Lett* 89:043115. <https://doi.org/10.1063/1.2235925>
57. Sun X, Qiao L, Pang H, Li D (2017) Synthesis of nanosheet-constructed SnO<sub>2</sub> spheres with efficient photocatalytic activity and high lithium storage capacity. *Ionics* 23:3177–3185. <https://doi.org/10.1007/s11581-017-2115-9>
58. Xie Y, Hu D, Liu L, Zhou P, Xu J, Ling Y (2016) Oxygen vacancy induced fast lithium storage and efficient organics photodegradation over ultrathin TiO<sub>2</sub> nanolayers grafted graphene sheets. *J Hazard Mater* 318:551–560. <https://doi.org/10.1016/j.jhazmat.2016.07.046>
59. Sun X, Si W, Liu X, Deng J, Xi L, Liu L, Yan C, Schmidt OG (2014) Multifunctional Ni/NiO hybrid nanomembranes as anode

- materials for high-rate Li-ion batteries. *Nano Energy* 9:168–175. <https://doi.org/10.1016/j.nanoen.2014.06.022>
60. Xie W, Wang Q, Xu J, Yu Y, Zhao R, Li N, Li M, Du Y, Peng S, Cao G (2019) Microbelt-void-microbelt-structured SnO<sub>2</sub>@C as an advanced electrode with outstanding rate capability and high reversibility. *J Mater Chem A* 7:10523–10533. <https://doi.org/10.1039/c9ta00527g>
61. Su L, Xu Y, Xie J, Wang L, Wang Y (2016) Multi-yolk-shell SnO<sub>2</sub>/Co<sub>3</sub>Sn<sub>2</sub>@C nanocubes with high initial coulombic efficiency and oxygen reutilization for lithium storage. *ACS Appl Mater Interfaces* 8:35172–35179. <https://doi.org/10.1021/acsami.6b10450>
62. Sun X, Hao G-P, Lu X, Xi L, Liu B, Si W, Ma C, Liu Q, Zhang Q, Kaskel S, Schmidt OG (2016) High-defect hydrophilic carbon cuboids anchored with Co/CoO nanoparticles as highly efficient and ultra-stable lithium-ion battery anodes. *J Mater Chem A* 4:10166–10173. <https://doi.org/10.1039/c6ta03098j>
63. Hu L, Zhong H, Zheng X, Huang Y, Zhang P, Chen Q (2012) CoMn<sub>2</sub>O<sub>4</sub> spinel hierarchical microspheres assembled with porous nanosheets as stable anodes for lithium-ion batteries. *Sci Rep* 2:986. <https://doi.org/10.1038/srep00986>
64. Wang L, Chen S, Hei J, Gao R, Liu L, Su L, Li G, Chen Z (2020) Ultrafine, high-loading and oxygen-deficient cerium oxide embedded on mesoporous carbon nanosheets for superior lithium-oxygen batteries. *Nano Energy* 71:104570. <https://doi.org/10.1016/j.nanoen.2020.104570>
65. Jamnik J, Maier J (2003) Nanocrystallinity effects in lithium battery materials aspects of nano-ionics. *Phys Chem Chem Phys* 5:5215–5220. <https://doi.org/10.1039/b309130a>
66. Kim H-S, Cook JB, Lin H, Ko JS, Tolbert SH, Ozolins V, Dunn B (2017) Oxygen vacancies enhance pseudocapacitive charge storage properties of MoO<sub>3-x</sub>. *Nat Mater* 16:454–460. <https://doi.org/10.1038/nmat4810>

**Publisher's note** Springer Nature remains neutral with regard to jurisdictional claims in published maps and institutional affiliations.